Eur. Phys. J. D **31**, 69–76 (2004)
DOI: 10.1140/epjd/e2004-00129-8

THE EUROPEAN PHYSICAL JOURNAL D

Structural, compositional, optical and colorimetric characterization of TiN-nanoparticles

A. Reinholdt[1,a], R. Pecenka[1], A. Pinchuk[1,2], S. Runte[1], A.L. Stepanov[1,3], Th.E. Weirich[4], and U. Kreibig[1]

[1] I. Physikalisches Institut 1A, RWTH Aachen, Postfach, 52056 Aachen, Germany
[2] Institute of Surface Chemistry of NASU, General Naumov Str. 17, 03164 Kyiv, Ukraine
[3] Institut für Experimentalphysik, Karl-Franzens-Universität, Universitätsplatz 5, 8010 Graz, Austria
[4] Gemeinschaftslabor für Elektronenmikroskopie, RWTH Aachen, Ahornstrasse 55, 52074 Aachen, Germany

Received 3 June 2004 / Received in final form 23 August 2004
Published online 28 September 2004 –

Abstract. We present results of an investigation of TiN nanoparticles, which were produced by laser ablation/evaporation and adiabatic expansion with the nanoparticle beam apparatus LUCAS. Compositional and structural characterization, using secondary ion mass spectrometry (SIMS), electron energy loss spectroscopy (EELS), X-ray diffraction (XRD) and selected area electron diffraction (SAED), revealed that crystalline and almost stoichiometric particles were formed and that they are susceptible to oxidation. Furthermore, transmission electron microscopy (TEM) analysis showed that TiN nanoparticles exhibit cuboid shapes. The size distributions were obtained using the edge length as parameter. They are fairly broad and the mean particle diameter depends on the seeding gas flow (the pressure) that is applied to the ablation chamber during production. In situ optical transmission spectra of the TiN nanoparticles deposited on a quartz substrate indicate a pronounced single Mie resonance at around 1.7 eV and an absorption flank starting at approximately 3.0 eV. The experimental optical extinction spectra of different samples were fitted using Mie theory calculations. The dielectric function of bulk TiN was modified to account for size and interface damping of the Mie resonance. Due to the distinct absorption band, TiN may be used as a color pigment. The dependence of the color stimulus on the extinction cross-section as well as on the product of the particle concentration and the sample thickness were examined. Chromaticity coordinates were derived according to the CIE 1976 ($L^*a^*b^*$) color space from the in situ optical transmission spectra.

PACS. 42.66.Ne Color vision: color detection, adaptation, and discrimination – 78.67.Bf Nanocrystals and nanoparticles – 81.07.Bc Nanocrystalline materials

1 Introduction

TiN and the other nitrides of the Ti-group gained much importance in the past, because of their special physical and chemical properties. They exhibit high hardness and abrasion resistance as well as high thermal stability and good conductivity. Today, they are used for example as hard and protective coatings for tools or in electronic devices.

Since the dielectric function is similar to a Drude-like metal, TiN also became interesting in nano-optics recently, because a pronounced Mie resonance should show up in the optical spectrum. This has been predicted by Quinten [1], who calculated nanoparticle spectra based on Mie's theory for monodisperse spherical particles. But to the best of our knowledge no experimental data has been published yet.

There is a constant search of new and stable color pigments for applications, because the widely used organic dyes tend to disintegrate in time or due to irradiation by UV light. Anorganic nanoparticles with distinct absorption bands can act as an alternative, because they often do not degrade in time. TiN in particular is suited for this application.

Besides the compositional and structural characterization, we focus in this article on the analysis and discussion of the optical and colorimetric properties. We present experimental extinction spectra and show, that they can be modeled by Mie theory calculations using a modified bulk dielectric function. In addition, the applicability of TiN as color pigment and the dependence of the color on different experimental parameters is discussed.

2 Experimental

The ablation target was produced from pressed TiN powder (Alpha Aesar, 99.8% purity). The powder was moistened with a few droplets of pure propanol and pressed for

[a] e-mail: reinholdt@physik.rwth-aachen.de

Table 1. Detailed data for the prepared samples. Φ is the N_2 seeding gas flow at normal pressure and d_{total} the total sample mass thickness. Samples with an asterisk (*) were used for colorimetric evaluations.

Sample	Φ [l/min]	d_{total} [nm]	Matrix
1	0.4	7.0	-
2	0.9	5.3	-
3	1.8	9.0	-
4	0.9	98.7	-
5	0.9	131.0	-
6	0.9	212.8*	MgF_2
7	0.9	180.3*	SiO_2
8	0.9	120.1*	Al_2O_3
9	0.9	165.5*	TiO_2
10	0.9	196.2*	SiO_2

about 10 min at approximately 2 kbar. The pellet was dried on air for several hours, allowing the propanol to evaporate.

The target was placed in the ablation chamber of the nanoparticle beam apparatus LUCAS [2,3]. It was ablated/evaporated by a LUMONICS JK702H Nd:YAG laser in an ambient nitrogen seeding gas atmosphere (Air Products, 99.99990% purity). The mean output energy was 1.5 J, the mean output power 120 W, the frequency 80 Hz, and the pulse duration 2 ms. A plasma plume emitting bright light formed above the target.

The effective mass thicknesses were determined by a quartz balance; d_{total} (see Tab. 1) denotes the final thickness of the samples.

For optical measurements of the deposited particles, three samples were prepared on a Suprasil 1 substrate (Aachener Quarz-Glas Technologie), each produced with a different seeding gas flow (see sample 1, 2 and 3 in Tab. 1 for details). Transmission spectroscopy was carried out by using a xenon arc lamp and a Zeiss MCS 400 multichannel spectrometer. Data acquisition was done by a computer using the ASPECT (Zeiss) program.

Simultaneously, carbon film coated copper grids, that had been mounted on the substrate, were covered with particles. The grids were carried ex situ after the experiment to the TEM laboratory. TEM analysis, including selected area electron diffraction (SAED) and electron energy loss spectroscopy (EELS), was carried out with a FEI TECHNAI F20 transmission electron microscope operated at 200 kV.

Further characterization was done on the 99 nm and the 131 nm thick TiN nanoparticle layer (samples 4 and 5 in Tab. 1), each covered by a MgF_2 protective top layer preventing oxidation. The former was used for chemical analysis by secondary ion mass spectrometry (SIMS). The secondary neutral particle fluxes were measured using the secondary ion mass spectrometer VG Microtech SIMS Lab 300 with electron beam post-ionization. The latter sample was examined by XRD using a Philips X'Pert PRO MRD X-ray diffractometer. The sample was irradiated by a Cu-K_α beam ($\lambda = 0.1542$ nm) with grazing incidence (1° incidence). A proportional detector with a parallel plates collimator was used.

A third set of samples (numbers 6−10) was prepared to investigate the colorimetric properties of the TiN nanoparticles. These samples were grown in a sandwich-like manner with alternating layers of matrix material and particles to combine sufficiently large thickness with low particle packing density. For embedding MgF_2, Al_2O_3, SiO_2, and TiO_2 were alternatively used. Optical spectra were recorded for every new embedded nanoparticle layer and the colorimetric properties were obtained using the program MQCOLOR by Quinten [4].

3 Colorimetry

3.1 The CIE 1976 (L*a*b*) color space

This section presents a brief overview of the colorimetric theory, that was used to calculate chromaticity coordinates. All values and calculations are given for the 2° standard colorimetric observer. The definitions are based on the proposals of the Commission Internationale de l'Éclairage (CIE) [5].

The CIE 1976 ($L^*a^*b^*$) color space (CIELAB color space) [5] is based upon the CIE 1931 standard colorimetric system. It mainly consists of the tristimulus values X, Y and Z, which are derived from the color stimulus function $\varphi(\lambda)$ by the following set of equations:

$$X = k \int_{\lambda_1}^{\lambda_2} \varphi(\lambda)\bar{x}(\lambda)d\lambda, \tag{1}$$

$$Y = k \int_{\lambda_1}^{\lambda_2} \varphi(\lambda)\bar{y}(\lambda)d\lambda, \tag{2}$$

$$Z = k \int_{\lambda_1}^{\lambda_2} \varphi(\lambda)\bar{z}(\lambda)d\lambda. \tag{3}$$

For secondary light sources (reflecting or transmitting objects), which are treated in this article, the color stimulus function is the product of the spectrum of the illuminant $S(\lambda)$ and the luminous factor $\beta(\lambda)$:

$$\varphi(\lambda) = S(\lambda)\beta(\lambda). \tag{4}$$

$\bar{x}(\lambda)$, $\bar{y}(\lambda)$, $\bar{z}(\lambda)$ are the color-matching functions which were defined by the CIE in 1931 and are shown in Figure 1. k is a normalization factor defined by

$$k = \frac{100}{\int_{\lambda_1}^{\lambda_2} S(\lambda)\bar{y}(\lambda)d\lambda}. \tag{5}$$

The three-dimensional, approximately uniform, rectangular coordinate system of the CIELAB color space consists of the brightness L^* and the chromaticity coordinates a^* and b^*. They are related to the tristimulus values X, Y,

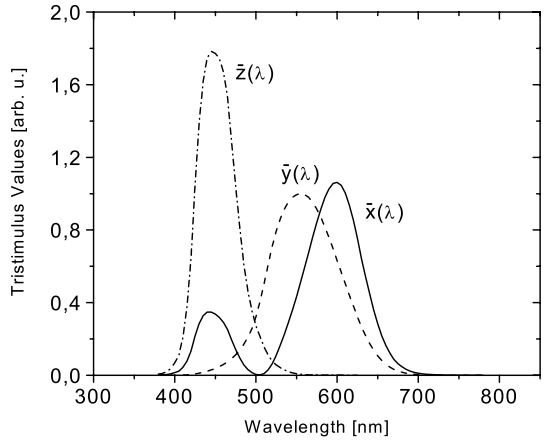

Fig. 1. Color-matching functions $\bar{x}(\lambda)$, $\bar{y}(\lambda)$, and $\bar{z}(\lambda)$ of the 2° standard colormetric observer [5].

and Z as follows:

$$L^* = 116\left(\frac{Y}{Y_n}\right)^{1/3} - 16, \tag{6}$$

$$a^* = 500\left[\left(\frac{X}{X_n}\right)^{1/3} - \left(\frac{Y}{Y_n}\right)^{1/3}\right], \tag{7}$$

$$b^* = 200\left[\left(\frac{Y}{Y_n}\right)^{1/3} - \left(\frac{Z}{Z_n}\right)^{1/3}\right]. \tag{8}$$

The values X_n, Y_n, and Z_n are the tristimulus values of the reference standard [5] that is illuminated by the light source used in the experiment. Thus, they differ for different illuminants.

For a quantitative comparison of two colors the quantity ΔE_{ab} is defined as the Euclidean distance between two color stimuli (i.e. two points) in the CIELAB color space:

$$\Delta E_{ab} = \sqrt{(\Delta L^*)^2 + (\Delta a^*)^2 + (\Delta b^*)^2}. \tag{9}$$

A value of $\Delta E_{ab} = 0$ means identical colors.

3.2 Changing the color stimulus

Since the color-matching functions $\bar{x}(\lambda)$, $\bar{y}(\lambda)$, and $\bar{z}(\lambda)$ are given and assuming that the illuminating light source will not be exchanged, the color stimulus of a sample only depends on the quantity $\beta(\lambda)$ (see Eq. (4)).

For optical transmission measurements $\beta(\lambda)$ equals the spectral transmittance:

$$\beta(\lambda) = \frac{I_t(\lambda)}{I_0(\lambda)} = \exp\left(-C_{ext}(\lambda) n z\right). \tag{10}$$

$I_t(\lambda)$ and $I_0(\lambda)$ are the intensities of the transmitted and the incident light accounting for reflection. $C_{ext}(\lambda)$ is the single particle extinction cross-section, n the volume concentration of particles in the sample and z its thickness.

One possibility to alter the color stimulus is to modify the extinction cross-section. For nanoparticles it is defined by Mie's theory [9] as

$$C_{ext} = \frac{2\pi}{|\mathbf{k}|^2}\sum_{L=1}^{\infty}(2L+1)\,\Re\left\{a_L + b_L\right\}, \tag{11}$$

where $\mathbf{k}$ is the wave vector of the incident light, L is the multipole order and a_L and b_L are the Mie coefficients [9].

In the quasi-static approximation (particle radius $R \ll \lambda$) this expression can be simplified for spherical particles as

$$C_{ext}(\omega) = 9\frac{\omega}{c}\varepsilon_M^{3/2} V \frac{\varepsilon_2(\omega)}{\left(\varepsilon_1(\omega) + 2\varepsilon_M\right)^2 + \varepsilon_2(\omega)^2}. \tag{12}$$

V is the volume of the particle, c the velocity of light and ω its angular frequency. The extinction cross-section and therefore the color stimulus can thus be influenced by either changing the dielectric function $\varepsilon(\omega) = \varepsilon_1(\omega) + i\varepsilon_2(\omega)$ of the particles or by embedding them into matrix materials, which have a different ε_M.

The color stimulus can also be altered by modifying the concentration of particles in the sample and/or varying the sample thickness. If $C_{ext}(\lambda)$ is left unchanged, the color of a sample is determined by the product

$$P = nz \tag{13}$$

(see Eq. (10)). That means, all combinations of n and z that lead to the same value of P result in the same color stimulus [1].

4 Results and discussion

4.1 Sample characterization

TEM investigations revealed a cuboid shape of the titanium nitride particles (Fig. 2). This indicates that the bonding inside the particles is not metallic, because spheroids or ellipsoids would be formed to minimize the surface energy. In fact, TiN has strong ionic and covalent contributions [6].

From the TEM images particle size distributions were obtained (Fig. 3). Because of the cuboid shape, we present the edge length L as parameter instead of the radius R. The distributions are fairly narrow.

As it can be seen from Table 2, the mean edge length enlarges monotonously with increasing seeding gas flow from $\langle L\rangle_1 = 6.5 \pm 0.1$ nm at $\Phi_1 = 0.4$ l/min to $\langle L\rangle_3 = 7.6 \pm 0.1$ nm at $\Phi_3 = 1.8$ l/min, flows calibrated to 1 bar. Due to the relatively broad distributions, the standard deviations are quite large with $\sigma_1 = 2.1$ nm, $\sigma_2 = 2.4$ nm, and $\sigma_3 = 1.2$ nm. The given errors of the mean, however, are very small due to the high number of counted particles.

The chemical composition of particles both protected against oxidation and exposed to air was determined using SIMS (Fig. 4) and EELS (Fig. 5), respectively.

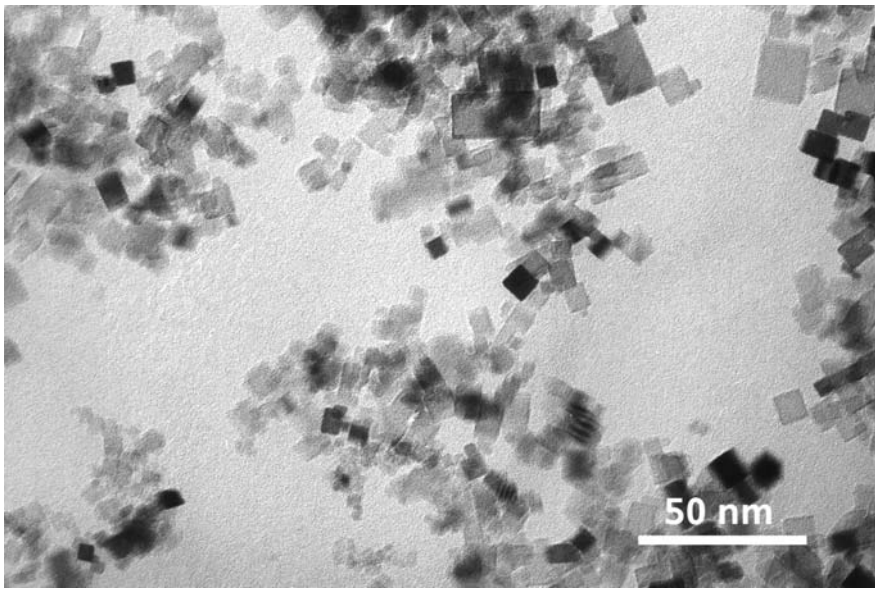

Fig. 2. TEM brightfield image of a TiN sample produced at $\Phi = 0.4$ l/min.

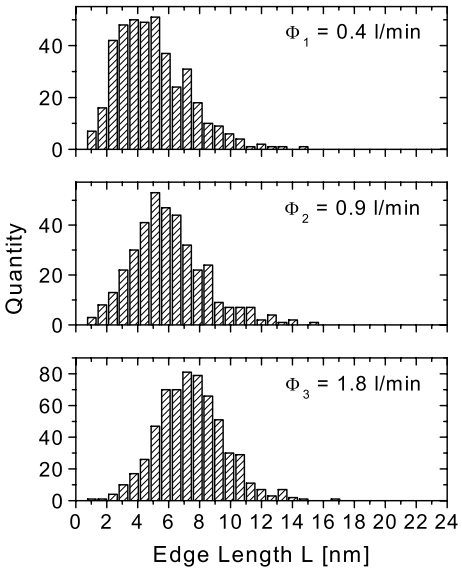

Fig. 3. Edge length distribution of the samples prepared with flows of $\Phi_1 = 0.4$ l/min, $\Phi_2 = 0.9$ l/min, and $\Phi_3 = 1.8$ l/min at normal pressure, respectively.

Table 2. Results of the analysis of the particle size distributions shown in Figure 3. Φ denotes the seeding gas flow, $\langle L \rangle$ is the sample mean, σ the empirical standard deviation and $\Delta(L) = \sigma/\sqrt{n}$ (n number of particles counted) the error of the mean.

Φ [l/min]	$\langle L \rangle$ [nm]	σ [nm]	$\Delta(L)$ [nm]
0.4	6.5	2.1	±0.1
0.9	6.8	2.4	±0.1
1.8	7.6	1.2	±0.1

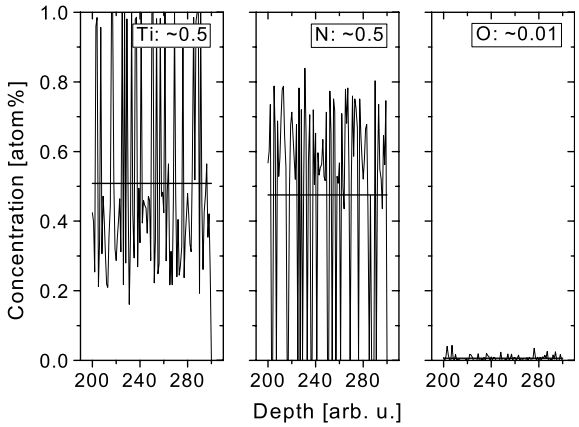

Fig. 4. Graphs of the three detected specimen using SIMS analysis. Since the signal is very noisy, average values for each specimen represented by the horizontal lines have been estimated, only. Using these average values the composition could be determined to be: Ti ≈ 0.5; N ≈ 0.5; O $\lesssim 0.01$.

Although the signal of the SIMS measurement is very noisy, an average of each signal was calculated. It is shown as horizontal line in each graph. Using these averages, the composition was determined to be: Ti ≈ 0.5; N ≈ 0.5; O $\lesssim 0.01$. Even though these values can only be rough estimates due to the small signal to noise ratio, it can be seen that the composition of the particles is approximately stoichiometric and that especially the fraction of oxygen is very small.

The EEL spectrum shows peaks at the Ti L3-, L2- and L1-edge as well as at the N K-edge. Moreover, appearance of the oxygen K-peak at 532 eV energy-loss indicates partial oxidation of the sample when exposed to ambient atmosphere.

It can be concluded that chemical reactions between the residual oxygen in the seeding gas and the titanium

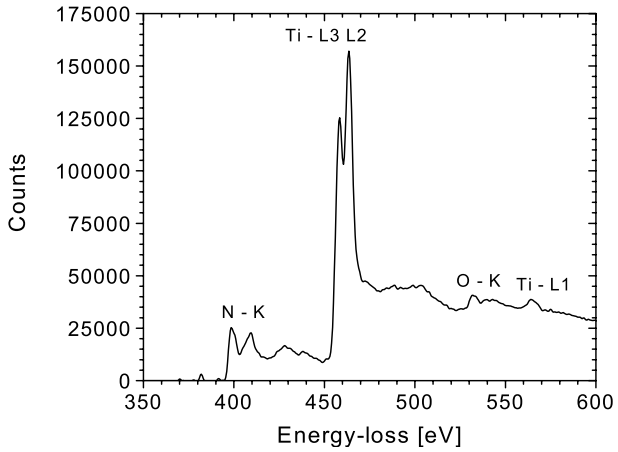

Fig. 5. Electron energy loss (EEL) spectrum of TiN nanoparticles.

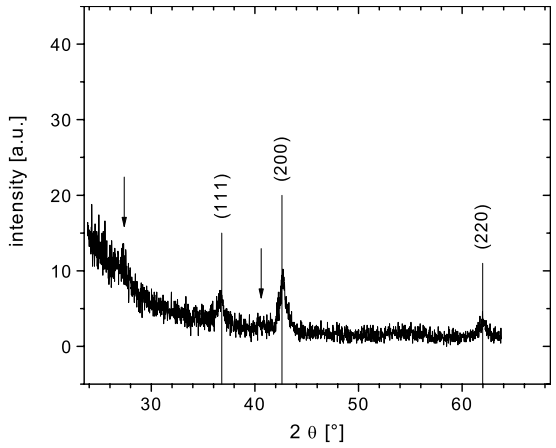

Fig. 6. XRD scan with grazing incidence (1° incidence) of the TiN-nanoparticle sample. The (111), (200), and (220) Bragg reflexes can clearly be observed. Their positions correspond to a fcc lattice (space group Fm3m) with a lattice parameter of $a \approx 4.24$ Å [7]. The features marked with an arrow at 27.3° and 40.5° correspond to the (110) and (111) peak of the MgF_2 protective top layer, respectively [8].

atoms are almost suppressed during production and the nitridation is favored under the given conditions. Exposure to a high partial pressure of oxygen, however, induces the formation of oxides and/or oxynitrides.

The results of the XRD measurements (see Fig. 6) show three pronounced Bragg reflexes at $2\theta_1 = (36.7 \pm 0.1)°$, $2\theta_2 = (42.7 \pm 0.1)°$, and $2\theta_3 = (62.0 \pm 0.1)°$, respectively. Using the JCPDS database, it could be verified that the peaks correspond to those of fcc-structured TiN ($2\theta_1 = 36.694°$, $2\theta_2 = 42.633°$, $2\theta_3 = 61.869°$; space group Fm3m) [7] with a lattice parameter of $a \approx 4.24$ Å. The structural properties are, hence, identical to those of the bulk within the limits of accuracy.

SAED was used to confirm these results. The analysis of the ring pattern shown in Figure 7 yielded the values $d_{hkl,exp}$ given in Table 3. They are in good agreement with those of bulk TiN (JCPDS 38-1420, shown in the same table). The fact that oxygen was present in the sample

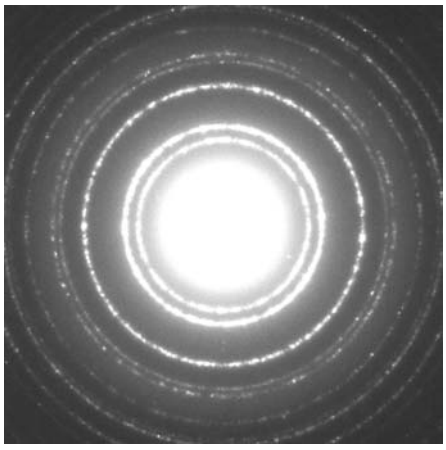

Fig. 7. Selected area electron diffraction pattern of TiN nanocrystals which reflects the typical sequence of rings of an F-centered lattice (see also Tab. 3).

Table 3. Values for the interplanar spacing for TiN nanoparticles: $d_{hkl,exp}$ denotes the values that were determined from analysis of the pattern shown in Figure 7. The error in determine the peak maxima of the rings is about ±1 percent. The reference data were taken from [7].

Ring	hkl	$d_{hkl,exp}$ [Å]	$d_{hkl,ref}$ [Å]
1	111	2.45	2.4491
2	200	2.10	2.1207
3	220	1.49	1.4996
4	311	1.28	1.2789
5	222	1.21	1.2244
6	400	1.05	1.0604
7	331	0.97	0.9730
8	420	0.94	0.9485
9	422	0.86	0.8658

due to previous exposure to air, does not seem to affect the positions of the rings.

4.2 Optical properties

The experimental optical extinction spectra, presented in Figure 8 as continuous lines, were derived from the in situ transmission data by using the Lambert-Beer law [9,10]:

$$E = -\ln(I_t/I_0) = C_{ext} n z. \tag{14}$$

I_t is the intensity of the transmitted and I_0 the intensity of the incident light.

All three spectra exhibit a pronounced band as well as a steep absorption flank, that can be ascribed to electronic interband transitions. Fitting the peaks with a Lorentzian curve, the data shown in Table 4 were obtained.

The resonance maximum positions vary from $\hbar\omega_{max,1} = 1.79 \pm 0.01$ eV for the first to $\hbar\omega_{max,3} = 1.65 \pm 0.01$ eV for the third sample. It should be noted, that, within the margin of error, the resonance maximum

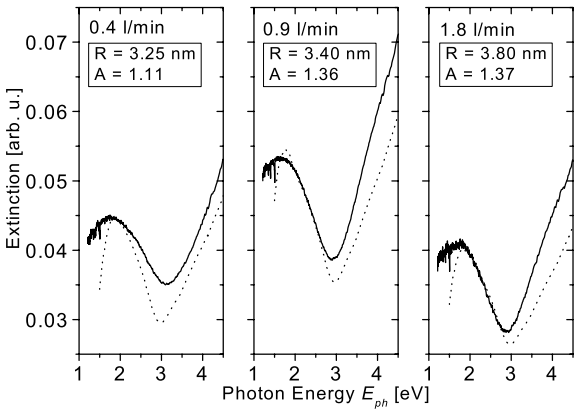

Fig. 8. Optical extinction spectra of TiN nanoparticles. The continuous lines show the experimental data and the dashed ones the calculations. In each figure the respective seeding gas flow and the parameters used for the calculation (box) are shown.

Table 4. Resonance frequencies and HWHM values for the spectra shown in Figure 8.

Φ [l/min]	$\hbar\omega_{max}$ [eV]	$\Gamma/2$ [eV]
0.4	1.79 ± 0.01	1.21 ± 0.05
0.9	1.63 ± 0.01	1.05 ± 0.05
1.8	1.65 ± 0.01	0.95 ± 0.05

positions for the second and third sample are approximately the same ($\hbar\omega_{max} \approx 1.64$ eV). The high energy half of the band width (HWHM) $\Gamma/2$ clearly lessens towards the last spectrum from $\Gamma_1/2 = 1.21 \pm 0.05$ eV to $\Gamma_3 = 0.95 \pm 0.05$ eV. This is, most probably, caused by the decreasing portion of small particles.

To model the experimental data, the particles were approximated by spheres with $R = \langle L \rangle/2$ (concerning the problems involved, see [9]). Mie calculations [9] for monodisperse particles were performed according to equation (11) with the dielectric function of TiN taken from [11]. Since the particle sizes are smaller than the mean free path of the electrons, additional damping had to be considered [12,13]:

$$\varepsilon(\omega) = 1 - \frac{\omega_p^2}{\omega\,(\omega - i\gamma)} + \chi^{ib}. \tag{15}$$

Here, ω_p is the Drude plasma frequency and χ^{ib} is the complex contribution to the susceptibility accounting for interband transitions. The adjusted damping constant

$$\gamma = \gamma_{bulk} + A\frac{v_F}{R} \tag{16}$$

consists of the bulk value γ_{bulk} as well as of a term that is proportional to the Fermi velocity v_F divided by the particle radius R. The parameter A comprises the additional damping, which is influenced by the interface and the size of the particles:

$$A = A^{size} + A^{interface}. \tag{17}$$

With the damping constant $\gamma_{bulk} = 0.75$ eV and the Fermi velocity $v_F = 1.39 \times 10^6$ m/s for TiN (taken from [14]), the results shown as dashed lines in Figure 8 were obtained. The given A-parameters are optimized to fit the *total* experimental curves including the high frequency interband edge. Hence, the maximum and minimum positions differ slightly.

One can clearly see, that the peak maxima of the calculated spectra are in fairly good agreement with the experimental data. The peak widths, however, are too small. That means, additional damping takes place in the particles, which could not be modeled by fitting with the A-parameter. There are mainly three effects, we assume to be responsible for the deviations.

First, the particles have cuboid shapes. This leads to special edge and corner modes in the particles [9]. The additional resonances will smear out the spectrum and broaden the peak compared to spherical particle shapes.

Second, the particles are fairly narrowly packed (see Fig. 2) and the distances between them are within the region where electromagnetic coupling takes place. This also leads to broadening of the resonance [9].

The TEM studies showed that broad but loosely packed aggregates are present, however, coalescence does not occur. Extended Mie theory calculations with analogous spherical particles give way to estimate the effects of aggregation on peak position and width. They have not been performed, yet, mainly because the electrodynamic coupling between cuboids and between spheres differs strongly due to different aggregate modes caused by touching of planes, edges and corners of the cuboids.

Third, the calculations were carried out for a monodisperse size distribution, but, in fact, the samples are polydisperse (see Fig. 3). Thus, the measured spectrum is broadened compared to the theoretical result and, also, a slight too high A-parameter was obtained. In a forthcoming paper this problem will be treated in detail.

The influence of the substrate was neglected in the simulation. Earlier own calculations (not presented here) showed that the spectra only change slightly when the interaction between substrate and particles is taken into account, compared to the mentioned effects.

For the calculated interband transitions one can observe significant mismatches for all samples. This is up to the fact, that the susceptibility accounting for the interband transitions was assumed to be size-independent ($\chi^{ib} \neq \chi^{ib}(R)$), which may not be true for our nanoparticles. In principle, one could include the size dependence of χ^{ib} using e.g. density functional theory (DFT). But until now there has not been any published effort to approach this problem. Additionally, chemical impurities in the particles may influence the interband transitions.

4.3 Colorimetric analysis

4.3.1 Different matrix materials

The TiN nanoparticles were embedded into MgF_2, SiO_2, Al_2O_3, and TiO_2 (samples 6−9) in a sandwich-like manner

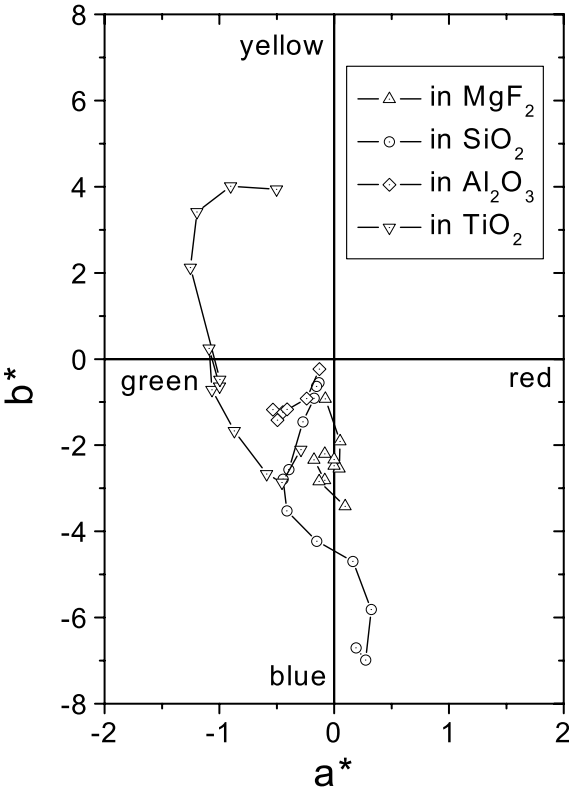

Fig. 9. Influence of the dielectric function of the embedding material on the color stimulus.

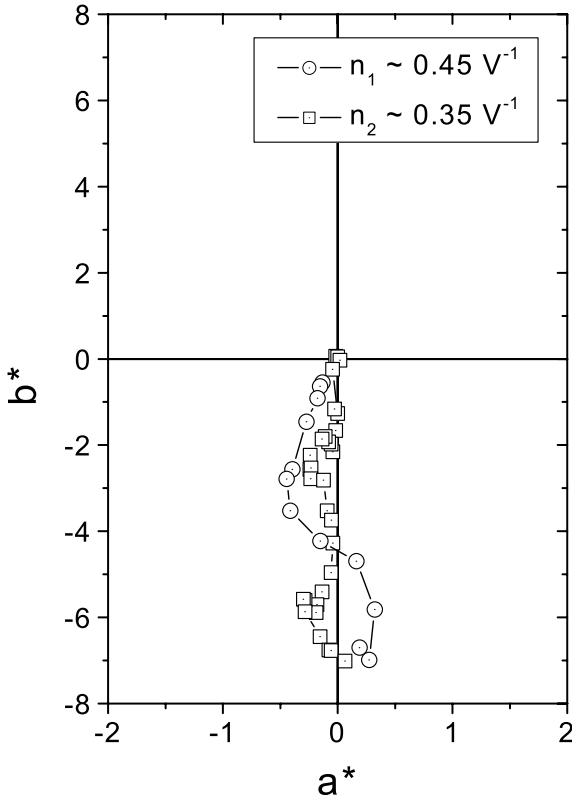

Fig. 10. Influence of the particle concentration on the color stimulus.

Table 5. Dielectric constant of the embedding materials in the VIS, as used in the experiment. The data were taken from [15]. For TiO_2 the values for the anatase (A) as well as the rutile (R) phase are shown.

	MgF_2	SiO_2	Al_2O_3	TiO_2 (A)	TiO_2 (R)
ε_M	1.932	2.211	3.129	6.559	8.410

as described before. The thickness of each layer was approximately 4 nm and the particle concentration was roughly kept constant at $n \approx 0.47((4\pi/3)\langle L\rangle^3)^{-1}$ in every sample. The colorimetric analyses of the optical transmission measurements, that were performed during preparation, are shown in Figure 9. For the sake of simplicity, the brightness L^* has been neglected and only a^* and b^* are plotted.

Two different effects on the color stimulus can be seen. First, along each curve the chromaticity coordinates are mainly determined by the quantity P (Eq. (13)), that means by the variation of z ($n \approx const.$). Second, the direction of each curve is determined by the change of the extinction cross-section $C_{ext}(\omega)$, as the embedding materials have different dielectric functions.

The effect for particles embedded in MgF_2 and SiO_2 is very similar due to the small difference in the dielectric function (see Tab. 5). In both measurements the curves run along the negative b^* axis towards blue. This changes strongly for increasing dielectric constants of the matrix. Already particles embedded in Al_2O_3, which has a moderately higher ε_M than MgF_2 and SiO_2, exhibit color stimuli with a higher amount of green. And for TiN particles embedded in TiO_2 the development is completely mutated. At small thicknesses of the sample the chromaticity coordinates develop as with the previous matrix materials. But beginning with $z \approx 12$ nm, there is a turning point and the direction is changed towards yellow. That means, the higher the dielectic constant of the matrix material is, the stronger is its effect on the color stimulus.

Especially with the last measurement one can see a common feature of all four curves, which was predicted by Quinten [1]. There is always a turning point, where the color stimuli turn back to the achromatic point (the origin).

4.3.2 Variation of the particle concentration

TiN nanoparticles were embedded in a sandwich-like manner in SiO_2 with two different concentrations (sample 7: $n_1 \approx 0.45V^{-1}$, sample 10: $n_2 \approx 0.35V^{-1}$, with $V = (4\pi/3)\langle L\rangle^3$), but under the same conditions (i.e. $C_{ext}(\omega) \approx const.$). The final mass thickness of TiN nanoparticles in both samples summed up to $d_{final} \approx 48$ nm. The results of the colorimetric analyses are shown in Figure 10.

As one can see, the development of the color stimulus for both samples is very similar, as it is predicted by theory. Thus, in these samples, the color is only depending

on the value of P and not on the actual thickness or particle concentration. The slight deviations of the two curves are due to the fact that neither the particle concentration nor the film thickness could be controlled very accurately during experiment.

5 Summary

This article demonstrates the production of TiN nanoparticles by laser ablation/evaporation and adiabatic expansion with the help of the nanoparticle beam apparatus LUCAS.

It could be shown, using TEM, that the particles own cuboid shapes. This is because of the dominating ionic and covalent character of the bonding. The mean edge length of the particles enlarges with increasing N_2 seeding gas flow and the size distributions are fairly broad. Some aggregation appears inevitable.

Compositional and structural investigations were carried out both on densely packed particle films and TEM grids with low coverage. SIMS analysis of a sample protected against oxidation revealed an almost stoichiometric composition with a negligible oxygen fraction. Exposure of the TiN particles to air, however, causes partly oxidation of the material as shown by EELS analysis. The cubic structure (NaCl type, space group Fm3m) was proved by X-ray diffraction and selected area electron diffraction. The here determined lattice constant ($a \approx 4.24$ Å) is in good agreement with that of bulk titanium nitride.

In situ optical spectroscopy measurements indicated a single Mie resonance in the visible — probably a plasmon resonance — and a steep absorption flank that is ascribed to interband transitions. Mie theory calculations were applied to model the experimental data. Good agreement of the resonance positions was achieved by considering damping due to the limited size of the particles in the dielectric function. The band width differed, however, because of additional damping effects, that were not taken into account for the calculations. The interband transition could also not be modeled accurately, since the interband transition susceptibility had to be assumed to be size independent, which may not be the case with small particles.

It was shown, that TiN nanoparticles are applicable as color pigments and the color stimulus depends on the optical and geometrical properties of the composite sample. The color can either be changed by modifying the extinction coefficient (here: by embedding the particles in different matrix materials) or by applying different values of the product P of the particle concentration n and the sample thickness z. Measurements also could verify, that P and not the actual values of n and z is indeed the significant quantity for the color change.

We are grateful to the Deutsche Forschungsgemeinschaft for the support of A. Reinholdt (Project KR 637/15) and to the A. von Humboldt Foundation for the support of A.L. Stepanov. The authors would like to thank R. Detemple and H. Dieker, who carried out the SIMS and XRD measurements. A. Pinchuk gratefully acknowledges the support from the Alexander von Humboldt Foundation and INTAS.

References

1. M. Quinten, Appl. Phys. B **73**, 317 (2001)
2. A.L. Stepanov, M. Gartz, G. Bour, A. Reinholdt, U. Kreibig, Vacuum **67**, 223 (2002)
3. M. Gartz, *Clusterphysik mit LUCAS, einer neuartigen Nanoteilchen-Quelle höchster Leistung* (Wissenschaftsverlag Mainz, Aachen, 2001)
4. Vendor: `ulmi.quinten@t-online.de`
5. CIE, *Publication 15.2 – Colorimetry* (CIE, Vienna, 1986)
6. B.V. Reddy, S.N. Khanna, Phys. Rev. B **54**, 2240 (1996)
7. JCPDS database, 38-1420; W. Wong-Ng et al., Powder Diffraction **2**, 191 (1987)
8. JCPDS database, 70-2268
9. U. Kreibig, M. Vollmer, *Optical Properties of Metal Clusters* (Springer, Berlin, Heidelberg, 1995)
10. H.C. van de Hulst, *Light Scattering by Small Particles* (Dover Publications Inc., New York, 1981)
11. E.D. Palik, *Handbook of Optical Constants of Solids II* (Academic Press Inc., Boston, 1991)
12. B.N.J. Persson, Surf. Sci. **281**, 153 (1993)
13. A. Pinchuk, U. Kreibig, New J. Phys. **5**, 151.1 (2003)
14. J. Humlichek, A. Nebojsa, J. Hora, M. Strasky, J. Spoustac, T. Sikola, Thin Solid Films **332**, 25 (1998)
15. D.R. Lide, *CRC Handbook of Chemistry and Physics*, 78th edn. (CRC Press, Boca Raton, New York, 1997)